Neural computation through sensorimotor dynamics for predictive sensorimotor control

Running Title: Sensory-motor interplay in motor cortex

Yiheng Zhang[1,3,4], Yun Chen[1,3,4], Tianwei Wang[1,3], and He Cui[1,2,3]*

[1] Center for Excellence in Brain Science and Intelligence Technology, Institute of Neuroscience, Chinese Academy of Sciences, Shanghai 200031, China

[2] Shanghai Center for Brain and Brain-inspired Intelligence Technology, Shanghai, 200031, China

[3] University of Chinese Academy of Sciences, Beijing 100049, China

[4] equal contribution

*Correspondence: cuihe@ion.ac.cn

Highlights

- M1 neuronal activity is jointly tuned by reach direction and target motion during flexible manual interception.

- Neural states of single trials form an orbital neural geometry at movement onset.

- Neural geometry emerges in a recurrent neural network for predictive spatiotemporal transformation.

- Movement-related neural structures tilted by target motion result from mixed sensorimotor selectivity at the single-neuron level.

Summary

Although recent studies have shown that activity of the motor cortex conveys substantial information regarding sensory inputs in addition to motor outputs, it is unclear how sensory inflows and motor outflows interplay to issue motor commands. Here, we recorded population neural activity in the motor cortex via microelectrode arrays while monkeys performed flexible manual interception of moving targets, in a task that required predictive sensorimotor control. For such a dynamic sensory-motor task, the activity of most neurons in the motor cortex not only encoded upcoming movements, but was also modulated by ongoing target motion. Dimensionality reduction at movement onset demonstrated a latent orbital neural geometry with neural states clustered by reach directions, and tilted in ellipses corresponding to target speed. Such neural geometry also emerged in a recurrent neural network (RNN) with task-specific input-output mapping. We propose that neural computation through sensorimotor dynamics is based on neuronal mixed selectivity, and acts like a state evolution.

Keywords

Reach, Population Decoding, Dimensionality Reduction, Recurrent Neural Network, Motor Cortex

Introduction

Motor cortex, a central brain region generating motor commands, has been recently found to carry substantial sensory information (Hatsopoulos and Suminski, 2011; Sobinov and Bensmaia, 2021) in addition to movement kinetics (Evarts, 1968; Tanaka, 2016) and kinematics (Georgopoulos et al., 1982; Omrani et al., 2017; Wang et al., 2022). Activity in the motor cortex is strongly influenced by reference frame (Pesaran et al., 2006), hand trajectory (Paninski et al., 2004), and stimuli for target selection (Cisek and Kalaska, 2005); some neurons even respond to sensory stimuli alone during visual replay (Tkach et al., 2007). However, it is unclear how sensory inflows and motor outflows interact to form motor plans in the motor cortex.

With recent advances in large-scale neural recording and population analysis, a dynamical systems perspective has emerged in motor control that posits the motor cortex as an autonomous dynamical machine (Churchland et al., 2012; Shenoy et al., 2013; Vyas et al., 2020). From this point of view, preparatory population activity is promoted toward a movement-specific optimal subspace to set initial states seeding the motor generation (Churchland et al., 2010; Churchland et al., 2006). However, it remains to be determined if behaviorally relevant sensory variables are also embodied in the movement-related neural subspace, or in a separate/orthogonal one (Kaufman et al., 2014; Stavisky et al., 2017).

To reveal neural dynamics related to sensorimotor interplay, we recorded population activity in the primary motor cortex (M1) from monkeys performing a flexible manual interception task (Li et al., 2018; 2022). Unlike previous studies requiring interception at a fixed location (Merchant et al., 2004a; b), this flexible interception depends on predictive spatiotemporal mappings to displace a body effector to the right place at the right time. We found that the activity of most neurons was jointly tuned to both reach direction and target speed f as gain modulation, directional selectivity shifting, baseline adjustment, or their combinations. Strikingly, such mixed sensorimotor selectivity was exhibited throughout the entire trial, in contrast to the gradient of sensory-to-motor tuning from cue to movement epochs that we recently reported in posterior parietal cortex (PPC) (Li et al., 2022). Principal

component analysis (PCA) of the neural population revealed a clear orbital neural geometry in low-dimensional space at movement onset. Interestingly, the neural states were clustered by reach directions, and formed ringlike structures whose slopes were determined by target speed. A recurrent neural network (RNN) trained with proper input-output mappings demanded by the task could mimic such neural geometry. Further simulation indicated that these characteristics of neural population dynamics could be derived from the mixed sensorimotor selectivity of single neurons. We propose that neural computations through dynamics in latent space might provide deep insights into the sensorimotor interplay for predictive sensorimotor control.

Results

Behavioral task and performance

Three macaque monkeys (*Macaca mulata,* C, G, and D, male 7-10 kg) were trained to perform a delayed manual interception task (Figure 1A) modified from the task employed by (Li et al., 2018). The monkey held a dot in the center for 600 ms to initiate a trial, and then a static or circularly moving target appeared at a random location on a circular track centered on that dot. The monkey was required to wait for a random delay (400-800 ms) until the central dot went dark (GO signal), and then to immediately reach for the target. The target moved at one of five angular speeds either counterclockwise (CCW) or clockwise (CW) as -240 °/s, -120 °/s, 0 (static control), 120 °/s, and 240 °/s, interleaved trial by trial; it stopped once the monkey touched any peripheral location.

For well-trained monkeys, the reach was launched directly toward the target location at interception, with little in-flight adjustment (Figure 1B; (Li et al., 2018)). Behavioral performance across the five target-speed conditions was similar, with overlapped endpoint distribution (Figure 1B dot ellipses) and hand velocity profiles (Figure 1C, correlation coefficient 0.96±0.05, mean± SD). In this flexible interception task, the predictive motor plans guaranteed by the interleaved design along with the consistent performance across different conditions, enabled an efficient dissociation between sensory modulation and motor planning.

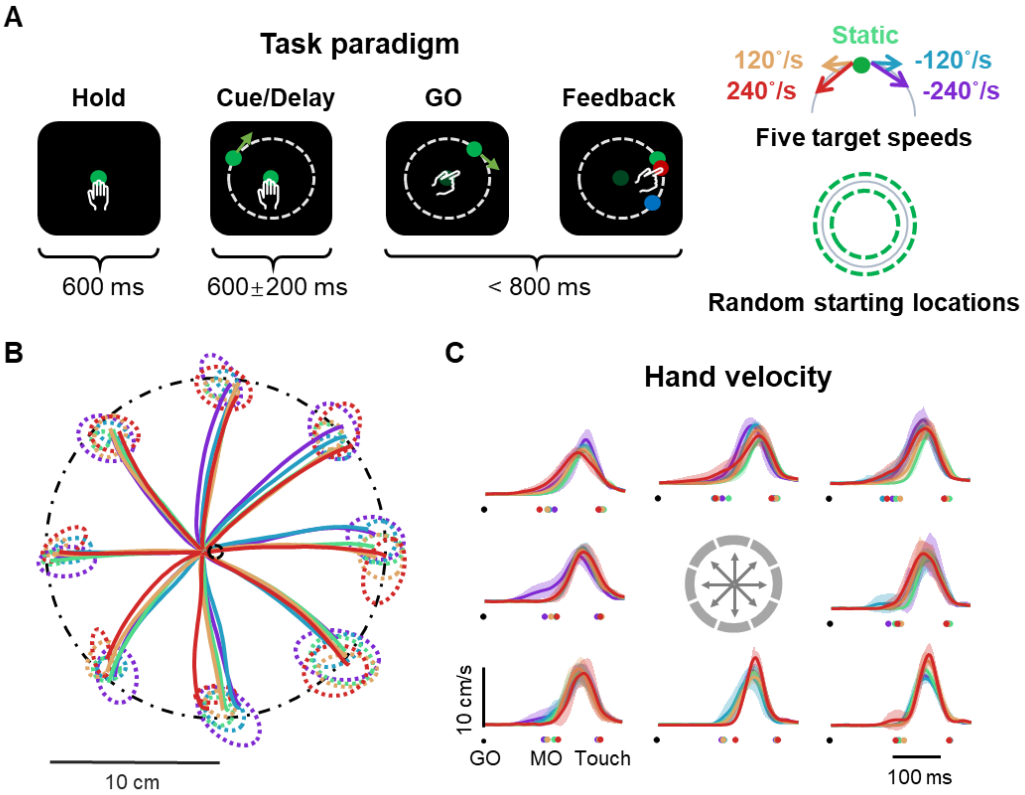

Figure 1. Flexible manual interception task and behavioral performance

(A) Diagram of interception task. The five target-speed conditions (-240 °/s, -120 °/s, static, 120 °/s, and 240 °/s) are indicated in five colors (red, yellow, green, blue, and purple). Target starting location was randomly distributed.

(B) The condition-averaged hand trajectory. The mean trajectories from MO to touch in five target-speed conditions (monkey C, 772 correct trials in one session) were plotted as solid lines in the same color as (A). Reach direction was divided into eight zones each covering 45 degrees, and represented by the corresponding eight directions. The distribution of reach endpoints relative to target endpoints is shown by the dot ellipses. The shifted center-holding was likely due to individual preference.

(C) The condition-averaged hand velocity. Hand velocity in the same session was averaged by both target speed and reach direction as in (B). The lines are in the same color as in (A) and the position of subplots corresponds to the reach direction denoted by gray inset. All profiles are aligned to GO (black dots) with marked movement onset (MO) and touch (interception) time (dots in colors).

Mixed sensorimotor selectivity of single neurons

Our first question is whether the directional selectivity of neurons in the motor cortex would be modulated by target speed. We recorded 95, 107, and 55 single neurons with Utah arrays from monkey C, G, and D, respectively (implanted sites were shown in Figure 2A). Notably, we found that neuronal directional tuning was affected by target motion mainly in three ways: preferred direction (PD) shift, gain modulation, and baseline adjustment (Figures 2B and S1-S3, Methods). Some neurons showed shifted PDs during interception of moving targets relative to the PDs of static targets (Figure 2B, *PD shift*). In this case, the motion direction rather than the speed of the target dominated the PD shift, as illustrated by an example neuron: its PDs corresponding to CCW conditions (red and yellow) were clearly distinguished from those of CW conditions (blue and purple), while its tuning curves for conditions with the same direction, namely 240 °/s (red) and 120 °/s (yellow) as well as -240 °/s (purple) and -120 °/s (blue), were very similar. Some neurons exhibited reach-direction tuning with gain modulation by target speed (Figure 2B, *gain*). Here the PDs remained invariant; instead, the neuronal responses at PD differed across conditions. This modulation was dominated by the direction of target motion as well. The turning curves of the example neuron, which displayed higher responses at PD in CW conditions (blue and purple) than in others (green, yellow, and red), implied a varying strength of selectivity for reach direction. In addition, the baseline activity of some neurons changed with target speeds (Figure 2B, *baseline*). As the adjustment was distributed uniformly in almost all reach directions, the target speed seemed like a scaling factor of neuronal activity.

It was difficult to classify these neurons with mixed sensorimotor selectivity into the three groups (PD shift, gain, and baseline) exclusively, because many of them exhibited mixed two or three of above modulations (Figure 2C). Moreover, there was no bias or clustering for neurons with certain combinations of modulations, making it hard to give an analytical description of single neurons. These results demonstrate heterogeneous patterns of sensorimotor interplay in M1 neurons, suggesting that the motor cortex is involved in complex sensorimotor computation.

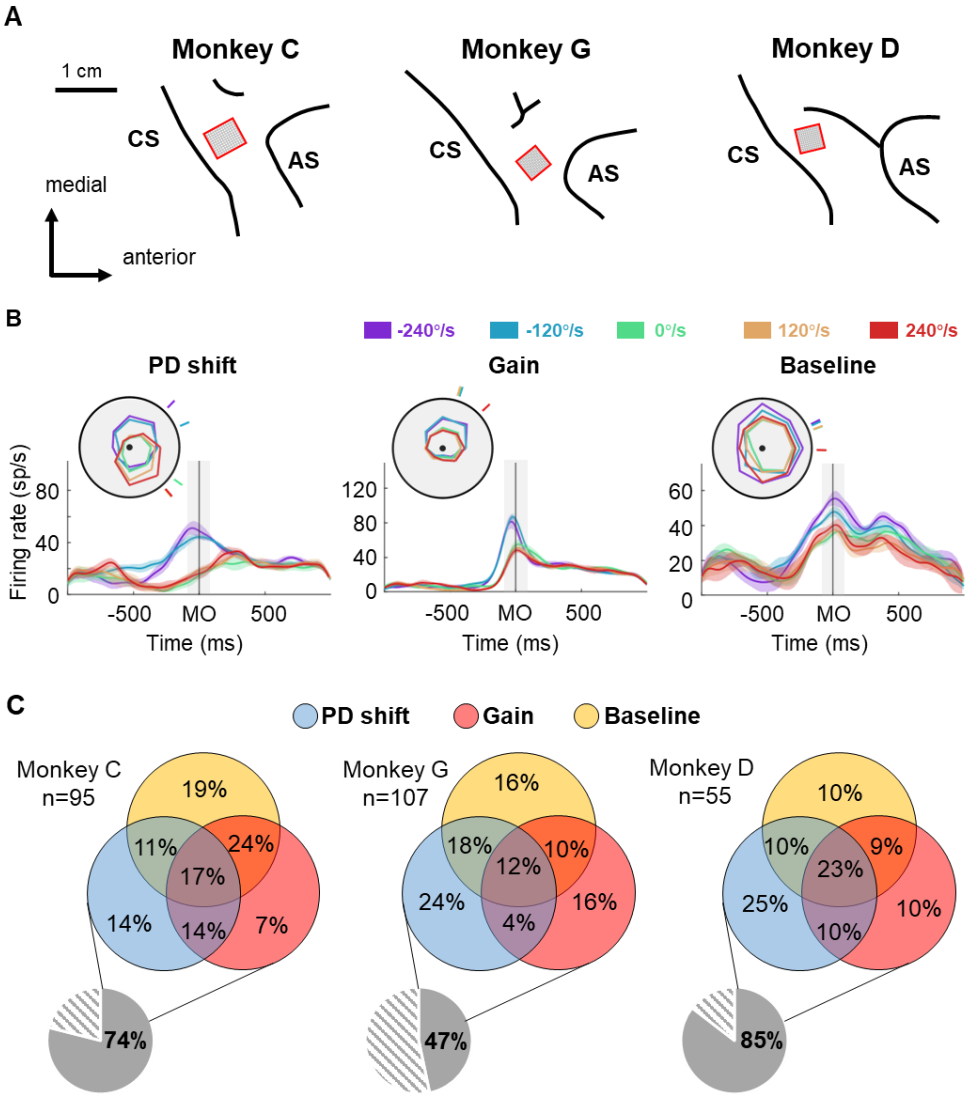

Figure 2. Mixed sensorimotor selectivity of single neurons

(A) Utah array locations in the motor cortex of the three monkeys. Neural data were collected with monkey using the hand contralateral to the recorded cortical regions. AS, arcuate sulcus; CS, central sulcus.

(B) Three example neurons with PD shift, gain modulation, and baseline adjustment, respectively. The peristimulus time histograms (PSTH) shows the activity of example neurons when monkeys reached to upper areas in five target-speed conditions. The inset as radar plot shows the reach tuning curves in polar coordinate system around the movement onset (± 100 ms), with surrounding short bars pointing to the preferred directions. The shadow area of PSTH lines denotes the standard error.

(C) The proportions of three types of modulation around MO of three monkeys. The small pie charts show the proportions of neurons with (gray) or without (shadow) sensory modulation. The large pie charts show the proportions of neurons with mixed sensorimotor selectivity specifically in PD shift (blue), gain modulation (red), baseline adjustment (yellow), or their mixture (overlapped).

Population decoding sensory and motor information

To learn more about sensorimotor computation during interception, we investigated the relevant information embodied in population activity. First, we performed a decoding analysis. Neural data from a selected session was utilized to train two support vector machine (SVM) classifiers for target speed (one in five) and reach direction (one in eight), respectively (Methods). As Figure 3A shows, the decoding accuracy of target speed rose quickly and peaked at over 70% around GO, while the decoding accuracy of reach direction climbed and reached a plateau of over 80% before movement onset (MO). Supported by this decoding result, the simultaneous encoding of target speed and reach direction from preparatory to execution period was also reflected at population level.

We wondered whether the encoding pattern varied with conditions, so we conducted a more detailed decoding analysis. In the resulting confusion matrices (Figure 3B), each patch denotes the decoding accuracy of a decoder trained by the row data and tested with the column data. It turned out that the reach-direction decoder could be generalized between static and interception conditions at GO and MO. This generalization, however, held for conditions with the same target motion direction (e.g., the -120 °/s trained classifier also worked for the -240 °/s condition), but not for conditions with opposite target motion directions (e.g., the -120 trained classifier was hard to decode 120 °/s or 240 °/s conditions). On the other hand, the target-speed decoder only showed temporal generalization between TO-GO and GO-MO, and was poorly generalized for the other reach directions. This result suggests that the population activity may reflect different coding strategies for reach direction and target speed.

Therefore, to explore these rules and determine how sensory inflow and motor outflow might interact at population level, we performed PCA on the normalized population activity. Figure 3C shows the neural states of single trials in different time windows. As MO approached, neural states gradually clustered by reach direction. The first two principal components (PCs) of the neural states at MO explained the most variance ([24.8%, 13.8%]) and were most related with reach direction (the mean fitting goodness of reach direction, $[R^2_{pc1},\ R^2{}_{pc2}]$ = [0.93, 0.86]). Furthermore, the neural states tended

to form five ringlike structures corresponding to five target speeds at MO (the mean goodness of fitting ellipses, R^2 = 0.67±0.06, 0.81±0.04, 0.93±0.01, and 0.77±0.05, for the four time windows, mean ± sd., Figure 3C). This inspired us to consider the possibility that the motor cortex encodes both reach direction and target speed information in a subtly structured manner at MO.

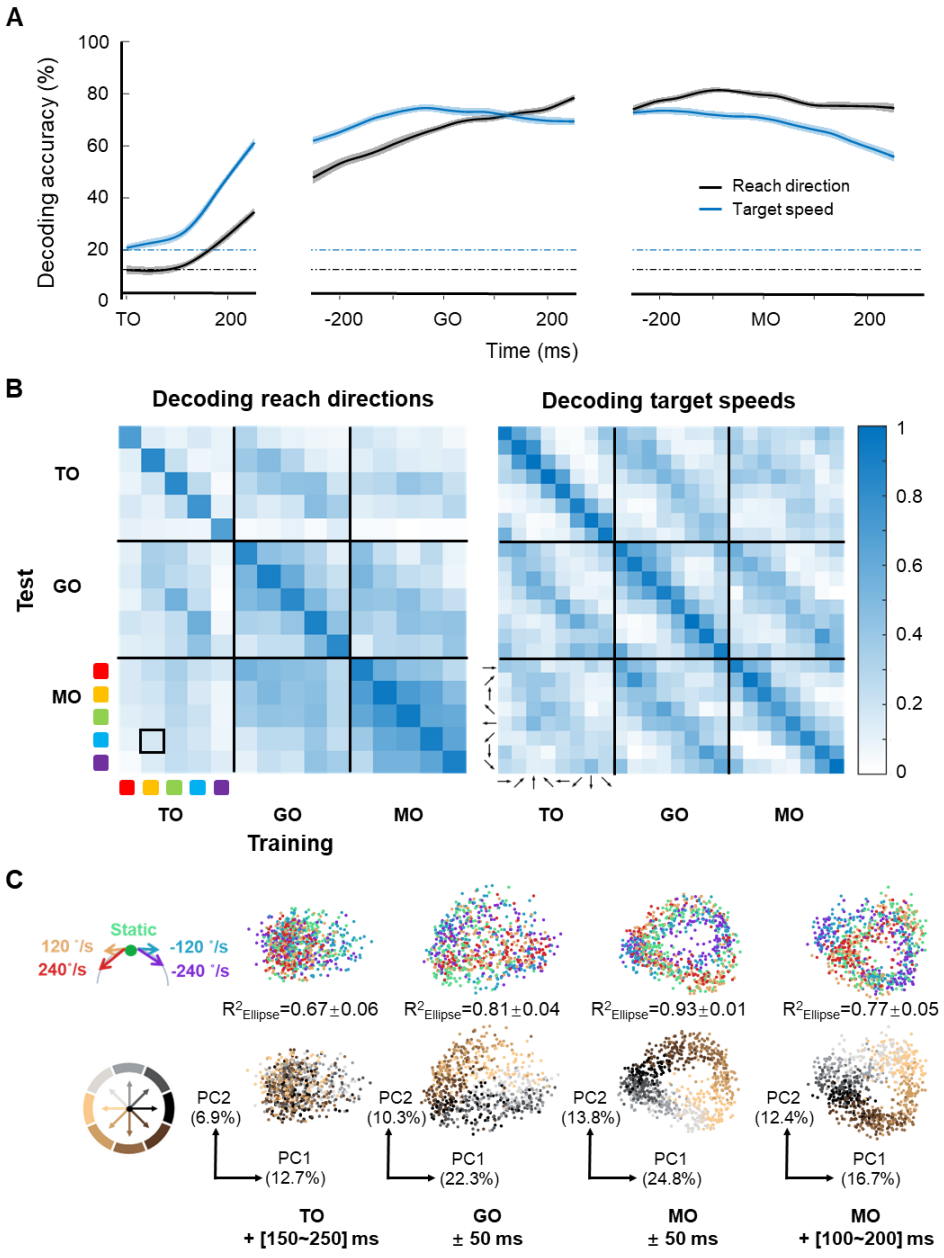

Figure 3. Features of encoding pattern at population level

(A) The mean decoding accuracy (SVM with 10-fold cross-validation) of reach direction (black solid line) and target speed (blue solid line) for population activity (monkey C, n=95, 100-ms sliding window), aligned to target on (TO), GO, and MO, respectively. The

dash-dotted lines are chance levels for reach direction (black, one in eight) and target speed (blue, one in five). The shaded area is the standard deviation.
(B) The decoding accuracy for reach direction and target speed in different conditions (the same dataset in Figure 3A). The left panel shows the decoding accuracy for reach direction among five target-speed conditions in three epochs: TO [200~400] ms, GO ± 100 ms, and MO ± 100 ms (SVM with 10-fold cross-validation, and the chance level is one in eight). The five target-speed conditions are labeled in five colored squares. The abscissa is the training data in one target-speed condition during one epoch, and the ordinate is the test data arranged in a consistent order. For example, the framed patch corresponds to a classifier trained by data in 120 °/s during TO and tested by -120 °/s during MO. The decoding accuracy is shown by the color depth. The right panel shows the decoding accuracy for target speed in distinct reach directions and time windows (SVM with 10-fold cross-validation, the chance level is one in five) with arrows with different direction indicating the reach direction.
(C) The neural states in different time windows. In the space spanned by the first two principal components (PCs), each point represents the neural state of a single trial and is colored in target speed (first row) or reach direction (second row). The corresponding explained variance of PCs and the R^2 of fitting ellipses is marked for different time windows.

The orbital neural geometry in latent dynamics

For a closer inspection, we focused on the newfound neural geometry in low-dimensional space at MO to examine the latent sensorimotor interaction. Then, we projected all neural states into the three-dimensional subspace resulted from static condition (Figures 4A and S4). Similar to the above two-dimensional results, the single-trial neural states clustered according to reach direction, and the projections of these clusters onto the PC1-PC2 subspace formed a ring in order (Figures 4A top and 4B right). Interestingly, the five ringlike structures of different target motion conditions, the 'target-speed ellipses' (R^2 = 0.92 ± 0.01, ellipse eccentricity = 0.59 ± 0.11, see Methods), exhibited organized nesting. They sloped with condition-dependent angles, which is particularly evident in the PC2-PC3 subspace (Figure 4A bottom and 4B left). This spatial feature was further quantified by calculating the elevation and azimuth angles of their normal vectors, which revealed that the ellipses of target speeds in opposite directions inclined symmetrically relative to the static condition, like mirroring (Figure 4C). We also fitted the 'PD' of individual PCs with cosine functions to show the tuning properties of three dimensions (Figure 4D). While the PDs of the first two PCs were similar across five target motion conditions (dash and dotted lines), the PDs of PC3 were quite different (solid lines), hinting that sensory information may be mainly embodied in PC3. This distribution agrees with the possible geometric description with parametric equations (Figure S5).

Given these results, we propose that this orbital neural geometry, including both the target-speed ellipses and the reach-direction clusters, epitomizes the sensorimotor interaction in the motor cortex at population level. This geometry maintained the principal and relatively robust neural coding of motor output during interception, even with different target speeds, via the reach-direction clusters ordered in the first two PCs. This geometry is also reflected in the target-speed ellipses, in which the sensory input can modulate the motor information in an orthogonal dimension (PC3), altering neural states without interfering with the generation of motor command.

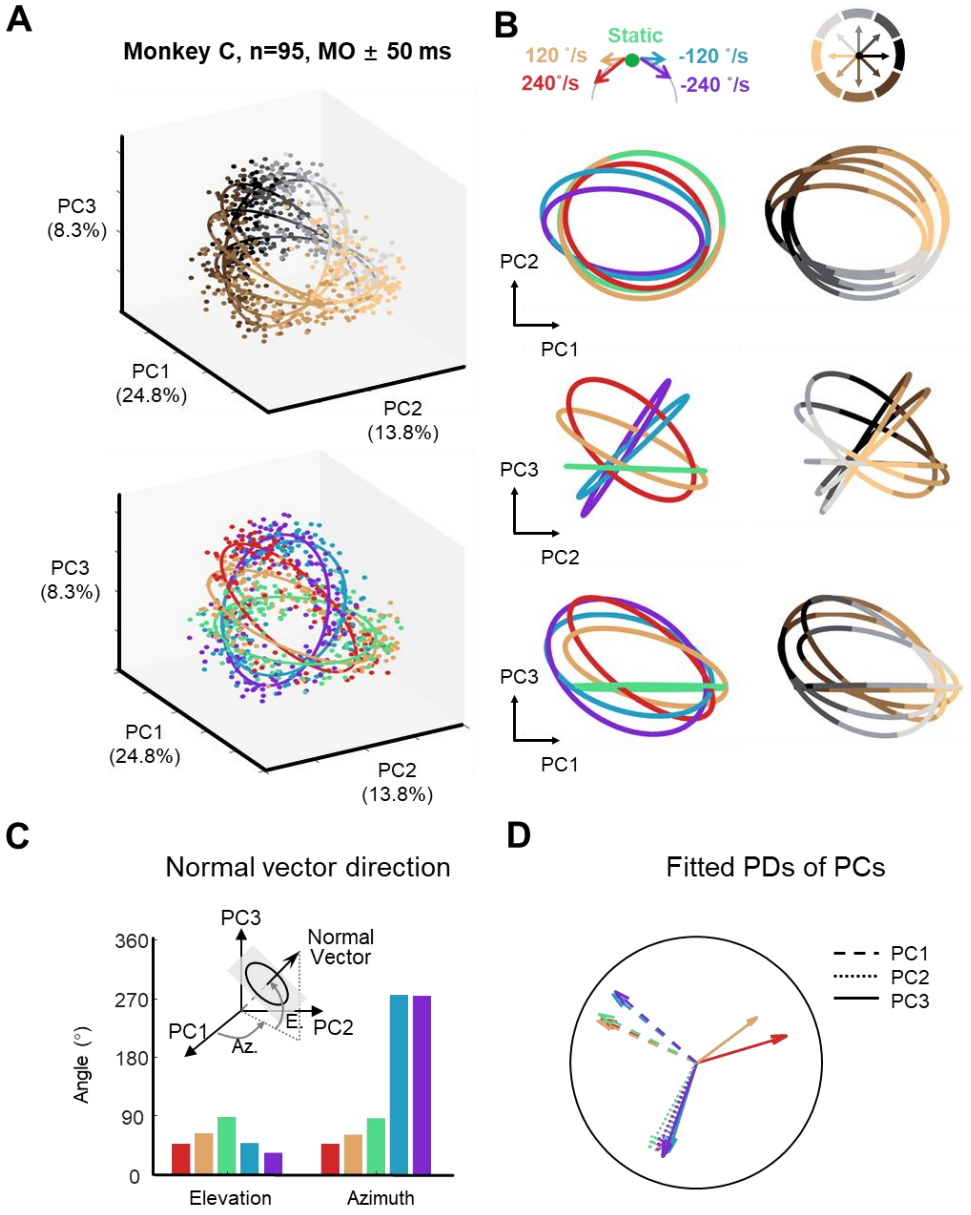

280

281 **Figure 4. The orbital neural geometry in latent dynamics**

282 (A) Three-dimensional neural state of M1 activity obtained from PCA. Similar to Figure
283 3C, each point represents a single trial. The upper subplot is colored corresponding to
284 five target speeds, while the bottom one is in colors corresponding to eight reach
285 directions. The explained variance of the first three PCs is 25.6%, 14.7%, and 8.7%,
286 respectively.

287 (B) Fitted ellipses of neural states. The ellipses fitted in (A) are projected onto three two-
288 dimensional spaces, colored in target speeds (left column) or reach directions (right
289 column).

290 (C) Elevation and azimuth angle of normal vectors of the fitted ellipses in (A).

291 (D) Fitted PDs of the first three PCs in five target-speed conditions. The goodness of
292 fitting is shown by the arrow length.

Recurrent Neural Network for dynamic input-output mappings

Even though the orbital neural geometry represents both sensory and motor information distinctly, it is notably a snapshot of dynamical evolution, rather than a constant representation (Figure 3C). We speculated that this neural geometry could be closely related to the initial states set in the optimal subspace. What kinds of external input may drive the neural dynamical system into such a state structure?

A series of RNNs receiving different combinations of inputs were built (Figure 5A; see Methods). The candidate inputs were simplified as target location, motor intention, and GO-signal to cover sensory, motor and timing information, respectively. In the brain, motor intention could be provided by the PPC (Andersen and Buneo, 2002; Andersen and Cui, 2009), and must be predictive to compensate for sensorimotor delays (Cui, 2016). We also compared the simulation effect of RNN with various forms of inputs. Although most variant networks could output accurate hand velocity, their state structure around MO appeared to diversely rely on input. For instance, in the absence of motor intention input, there were no reach-direction clusters in the state structure of the resulting network (Figure S7A); but one-dimensional stable or two-dimensional updating motor intention would cause the clusters to distort or disperse (Figures S7B and S7C). Moreover, if target location was offered as two-dimensional Cartesian coordinates, then the sensory modulation would not occur at the third PC, leading to a stack of target-speed-related state structures (Figure S7D). The network, whose state structure most resembled the orbital neural geometry, received target location in the real-time cosine of target direction, motor intention in stable two-dimensional Cartesian coordinates, and the GO signal in a step function (Figure 5B; see Methods). This is not by chance, but rather due to the angular distribution of target direction and the circular distribution of motor intention.

To verify that the orbital network geometry was indeed a computational structure rather than a training byproduct, we tested novel target speeds on the trained network. The result was that the network produced an extrapolating state geometry, where the new target-speed ellipses were interpolated between their ‘elders’ according to both direction and magnitude (Figure 5C). This generalization was also found in real neural states in several

additional sessions (Figure 5D). The reproduction of the orbital neural geometry by RNN suggests that this geometry can be derived from a specific input-output mapping, and incorporated into the dynamical systems perspective for motor control.

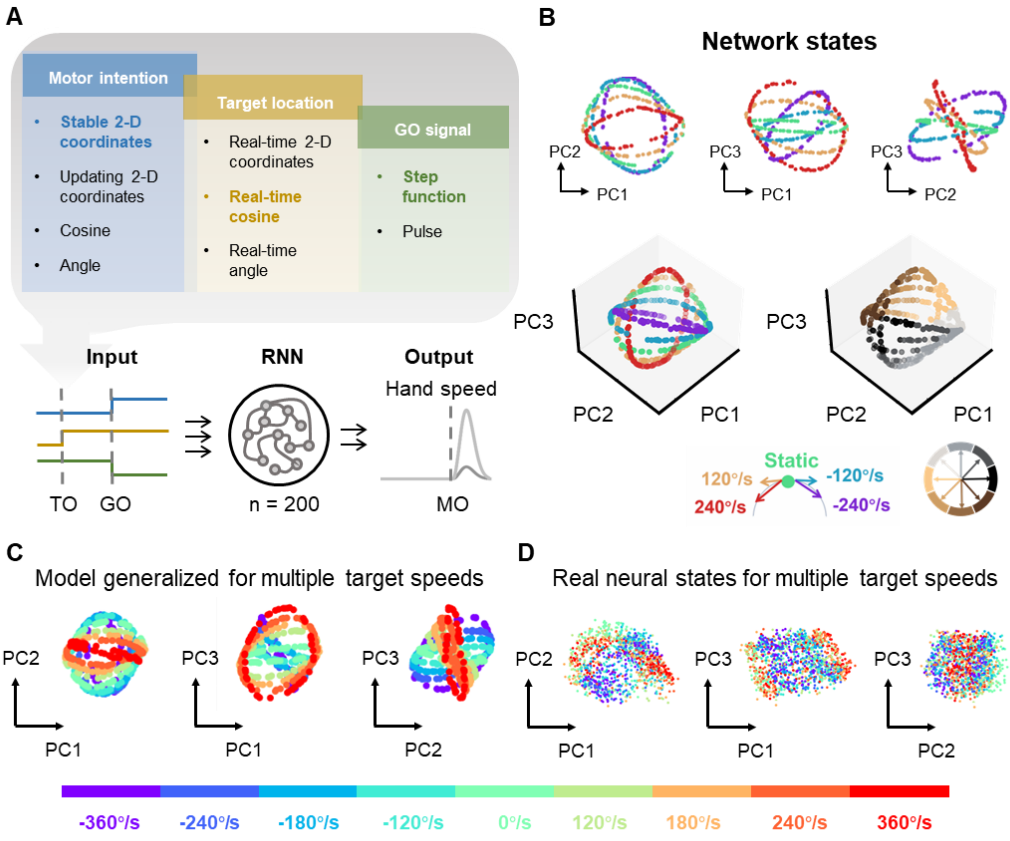

Figure 5. The neural geometry in RNNs

(A) RNN structure. The input of network contains different forms of motor intention, target location, and GO signal. The time flow for each input is also displayed. For each combination of inputs, the RNN with 200 hidden units is expected to output hand velocity for accurate interception.

(B) Network state geometry. The PCA results of RNN node activity result in a similar orbital geometry with neural data. Each point represents a trial and is colored according to target speed or reach direction (similar to Figure 4).

(C) The generalization to novel target speed in RNN. Network states are colored in target-speed conditions (color bar below). The ellipses for novel target speed are geometrically interpolated according to motion direction and speed magnitude of target.

(D) The generalization to novel target speed of real neural states (monkey C).

Population neural geometry relies on neuronal tuning

While the RNNs showed how special state geometry could dynamically emerge, another possibility was that the orbital geometry was also rooted in neuronal mixed sensorimotor selectivity. In this section, we probe whether a group of single neurons with some type of mixed sensorimotor selectivity can deliver the orbital neural geometry instantaneously, given motor intention and target speed.

For this purpose, three models for single neurons were deduced from the three typical modulations described above (PD shift, gain, and baseline, see Figure 2 and S1-S3), along with a full model designed to contain them all (Methods). We found that the adjusted R^2 of the full model (0.62±0.19) was larger than that of the PD shift model (0.2±0.19), gain model (0.55±0.19) and baseline model (0.47±0.24) for monkey C (n=95, rank-sum test, $p<0.01$, see examples in Figure 6A). The results were similar for the three monkeys (Figure S7B), again corroborating the mixture of patterns of sensorimotor selectivity on single neurons. Then, we ran a simulation with neuronal models. To clarify the effect of each modulation, we performed PCA on the activity of three groups of model neurons (Figure 6B). In the implementation, each group consisted of 200 model neurons with their PDs uniformly distributed, and was solely modulated by PD shift, gain, or baseline (Methods). The resulting neural geometry in the three simulation groups showed distinct features (Figure 6C): The five target-speed ellipses were inclined with condition-dependent angles in PD shift group and gain group, similar to the real data, but the ellipses in baseline group were layered in parallel. The reach-direction clusters in the first two PCs were preserved in the gain and baseline group, but not in the PD shift group. Therefore, only the gain modulation group could reproduce the desired orbital neural geometry.

The direct link of single-neuron selectivity with the shape of the population neural geometry, as suggested by our simulations, connects our understandings of sensorimotor interaction at different levels. From this, the gain modulation by sensory input on motor output appears to be a core characteristic, dominating the nonlinear sensorimotor interplay at movement

initiation during the dynamical process of interception.

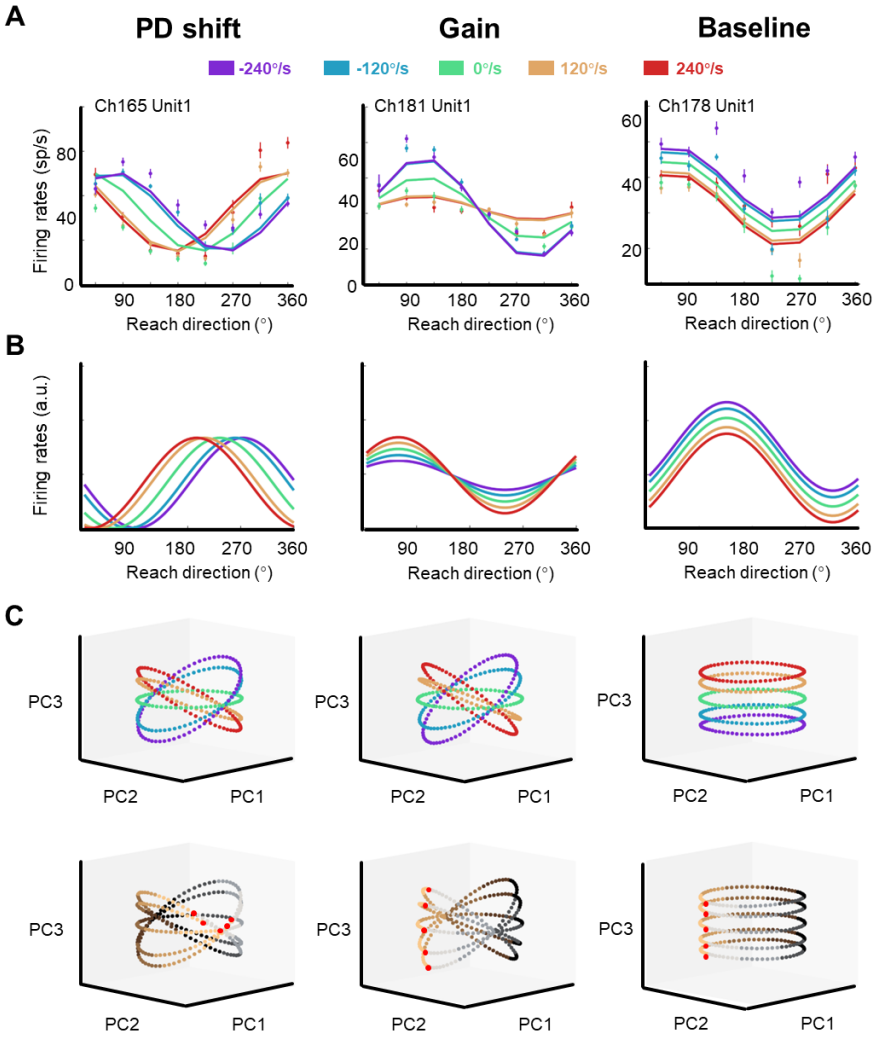

Figure 6. The shape of neural dynamics determined by neuronal mixed selectivity

(A) The activity of three example neurons with PD shift, gain, and baseline modulation (the same neurons as in Figure 2B). Dots and bars denote the average and standard error of firing rate under corresponding direction, colored in target-speed conditions. Lines show the fitted firing rates for corresponding models.

(B) The tuning curves of the three simulated neurons fitted by PD shift, gain, and baseline model, respectively.

(C) Neural states of population simulated neurons are shown in the space spanned by the first three PCs, colored by target speed or reach direction. Each population consists of 200 simulated neurons. The neural state in 180° reach direction is highlighted with a red marker. The first two PCs can explain more than 95% of the variance in the data. (Explained variance for the first three PCs, in PD shift: 50.1%, 47.1%, 1.6%; in Gain: 49.5%, 46.6%, 2.0%; in Baseline: 50.8%, 47.9% & 1.4%)

Discussion

To reveal how sensory inflows and motor outflows interplay in M1 to issue motor commands, we recorded population activity from monkeys performing a flexible manual interception that is highly dependent on predictive sensorimotor transformations. Single-neuron activity showed that the movement tuning of M1 neurons varied with target speeds in complicated ways, including PD shift, gain modulation, baseline adjustment, or their mixture. Dimensionality reduction on population activity revealed an orbital neural geometry with reach-direction clusters and tilted target-speed ellipses. Such a geometry, which also emerged in the RNN trained for appropriate input-output mappings, could be generalized to new target speeds. These results suggest that the neural mechanisms for predictive spatiotemporal transformation, especially during the interception in a dynamical context, stem from neuronal mixed sensorimotor selectivity, and can be visualized as a low-dimensional neural geometry compactly representing the sensorimotor interaction.

Dynamic sensorimotor interplay in the frontoparietal circuitry

Our investigation of the neuronal mixed selectivity was largely based on the efficient and systematic separation between sensory modulation and motor generation afforded by the behavioral paradigm (Li et al., 2018). The resulting movement endpoints distributed over the entire circle in our task enabled further scrutiny of the interaction between sensory and motor information, compared to that limited to a fixed touch point (Merchant et al., 2003). In addition, the regular target motion in our task resulted in similar behavioral characteristics, as opposed to the winding hand trajectories in the random pursuit task (Tkach et al., 2007). Therefore, unlike the interaction between motor efferent variables such as reach direction and hand velocity (Inoue et al., 2018; Moran and Schwartz, 1999; Paninski et al., 2004), or between sensory afferent parameters like gaze and head direction (Zipser and Andersen, 1988), our paradigm highlights an input-output interaction in the mapping from time-varying sensory input to definite motor output.

We speculate that this sensorimotor tuning reflects the ongoing flow of information in the frontoparietal network. The frontal and parietal areas are strongly interconnected and orchestrate many aspects of action planning (Andersen and Cui, 2009; Battaglia-Mayer and Caminiti, 2019). It is widely believed that the PPC plays a crucial role in the transformation from sensation to motor intention (Andersen and Buneo, 2002). In particular, area 7a has been reported to convey sensory information after the appearance of stimuli (Merchant et al., 2004a), while explicitly conveying intention about the forthcoming movement before interception (Li et al., 2022). In contrast, in this study, M1 encodes the reach direction in a sensory-modulated manner for almost entire trial (Figure 3). Taken together, these observations suggest that the sensorimotor integration occurs in circuits between the PPC and M1, as a part of the frontoparietal layered processing from intention to execution.

Sensorimotor computation in neural dynamics

In the orbital neural geometry, the sensory modulation seems to be presented in the third PC, whereas the motor information is captured by the first two PCs (Figure 4 and S5). This orthogonality of target speed relative to reach direction is consistent with the output-null hypothesis (Kaufman et al., 2014), which has also been supported by a study explaining how perturbation-evoked response avoided affecting the ongoing movement (Stavisky et al., 2017). Interestingly, it appears to be better explained in spherical coordinates than Cartesian coordinates, which is different from the previously described sensorimotor geometry (Remington et al., 2018).

Moreover, the maintenance of this neural geometry for more than 200 ms (Figure 3C, neural states around GO and MO) can be attributed to evolution from different initial states. The initial states are set by the preparatory activity in the motor cortex, which is promoted towards a movement-specific optimal subspace (Churchland et al., 2010; Churchland et al., 2006). As the motor cortex can be treated as an autonomous dynamical system (Churchland et al., 2012; Vyas et al., 2020), its evolution is hence influenced by initial states. In this case, the distribution of the initial states is hinted at by the orbital neural geometry, correspondingly featured by the reach-direction clusters and the tilted target-speed ellipses.

Neural geometry and neuronal mixed selectivity

As mentioned above, we found both mixed sensorimotor selectivity and the population orbital geometry in predictive sensorimotor control, raising the question of their relationship. A recent study has discussed this issue, and it proposed that the collective dynamics are flexibly shaped by the constitution of neural subpopulations with different selectivity and mainly driven by the complexity of the input-output mapping requirement of the performed task (Dubreuil et al., 2022). This provides an explanation for the differences among the neural geometries of three monkeys: The larger eccentricity (Figure S6A) and the more compressed structure (Figure S6B) of the five target-speed ellipses might both be related to the relatively lower proportion of the recorded neurons with mixed selectivity (44% and 52% vs. 66%, see Figure 2C). Furthermore, as the simulation result directly shows (Figure 6), a subpopulation with certain mixed selectivity can give corresponding features to their low-dimensional neural geometry, which implies that the dominant neuronal properties in the population can be estimated in turn.

Such neural geometry, however, may not be determined via pre-set computational procedures or by biological hierarchy, but may gradually emerge from the interplay between specific inputs and outputs (Pouget and Snyder, 2000). This can be evidenced by the reproduction of the orbital neural geometry in RNNs (Figure 5B). Thus, the motor plan for interception is likely to be generated from an interactive rather than hierarchical sensorimotor transformation.

Conclusions

A nonlinear sensorimotor interplay persistently occurs in the motor cortex during predictive sensorimotor control in dynamic circumstances, in this study in the form of an orbital neural geometry in population dynamics. Significant for the accomplishment of actions, such interaction comes from neuronal mixed selectivity and task-dependent input-output mapping. The present study adds to growing knowledge of dynamic sensorimotor processing; yet understanding more details may await the simultaneous recording of multiple cortical and subcortical regions and experimental interventions.

Acknowledgement

We thank C. Li, J. Mapleli, C. Zheng, and R. Zheng for helpful comments and discussions; C. Guan for veterinary assistance; and P. Ding, L. Du, and Z. Xiao for administrative support. This work was supported by National Key R&D Program (Grants 2020YFB1313400 and 2017YFA0701102), National Science Foundation of China (Grants 31871047 and 31671075), Shanghai Municipal Science and Technology Major Project (Grant 2021SHZDZX) and CAS Strategic Priority Research Program (Grant XDB32040103).

Author Contributions

Y. Zhang and H. Cui designed the experiment, Y. Zhang and T. Wang collected the data, Y. Zhang and Y. Chen analyzed the data, Y. Chen built RNNs, Y. Zhang performed the simulation, Y. Zhang, Y. Chen, T Wang, and H. Cui prepared the manuscript.

Declaration of interests

The authors declare no competing interests.

STAR Methods

RESOURCE AVAILABILITY

Lead Contact

Further information and requests for the data and codes should be directed to and will be fulfilled by the Lead Contact, He Cui (cuihe@ion.ac.cn).

Materials availability

This study did not generate new unique reagents.

Data and code availability

The datasets and code supporting the current study have not been deposited in a public repository but are available from the corresponding author on request.

EXPERIMENTAL MODEL AND SUBJECT DETAILS

Animals

Three adult male rhesus macaques (monkey C, D, and G, *Macaca mulatta*, 7-10 kg) were used in this study. The monkeys sat in a primate chair to perform the task. The stimuli were back projected onto a vertical touch screen (Elo Touch system, 19''; sampling at 100 Hz, spatial resolution <0.1 mm) about 30 cm in front of the monkeys. The hand trajectory was tracked by an optic camera (VICON Inc.) with an infrared marker on the fingertip. All the maintenance and procedures were in accordance with NIH guidelines and were approved by the CEBSIT Institutional Animal Care and Use Committee (IACUC).

METHOD DETAILS

Task and behavior

The monkeys were trained to perform a flexible manual interception task in a dark room. The task paradigm was modified based on the visually guided reaching interception task in a previous study (Li et al., 2018). At the beginning, the monkey held the green center dot of a touch screen for 600 ms

to initiate a trial (Figure 1A). Then, a green target dot appeared in a random location on the surrounding circle (invisible to the monkey) and started to rotate around the center. The center dot turned dark as a GO cue after a random delay (600±200 ms), then the monkey could intercept the target at any moment within 150-800 ms after GO cue. Once any peripheral location was touched, the target stopped. The tolerance range of the touch endpoint for correct trials is less than 2.5 cm away from the target. The monkey would be rewarded with juice after each correct trial. The target speed of clockwise -240 °/s, -120 °/s and counterclockwise 120 °/s, 240 °/s, as well as static, was pseudo-randomly interleaved trial by trial. More kinds of target speeds (-360 °/s, -180 °/s, 180 °/s, 360 °/s added) were introduced in the additional sessions.

Data collection

After the monkeys were adequately trained for the interception task (successful rate > 90%). Head-posts were implanted stereotaxically under anesthesia (introduced by 10 mg/kg ketamine, then sustained by 2% Isoflurane). After few weeks of recovery and adaptation, the monkeys were implanted with Utah microelectrode arrays (Blackrock Microsystems, Salt Lake City, UT) in the motor cortex of the hemisphere contralateral to the handedness (Figure 2A, 128-channel array for monkey C, 96-channel array for monkey G and D). The location of recording area referred to Magnetic Resonance Imaging (MRI) and cortical sulcus features. The neuronal activity was recorded by Blackrock Microsystem 256-channel recording system, sampled at 30 kHz. In the selected sessions, we collected 95, 107, and 55 well-isolate units of monkey C, G, and D, respectively.

QUANTIFICATION AND STATISTICAL ANALYSIS

Peri-stimulus time histograms (PSTHs)

The spike rasters and PSTHs of single neurons are shown in Figures 2B and S1-S3. All firing rates were calculated with 50-ms bin and smoothed with a Gaussian kernel (standard deviation = 20 ms). The standard error of firing rates was estimated from the 10 bootstrap samples in the trials of corresponding condition.

Classification of neuronal tuning properties

The preferred direction (PD) of each neuron for different target-speed conditions, in 100-ms bins, was calculated by the weighted sum of neuronal firing rates averaged in eight reach-direction conditions. The tuning depth of each neuron was determined by the range (max - min) of firing rates in corresponding condition. The baseline activity of each neuron was determined by the averaged neuronal firing rate in selected condition.

Based on the PD, tuning depth and baseline activity of single neurons, a neuron was classified as 'PD shift', if its PDs were significantly different between interception and static condition (Watson-Williams test in circular data, CircStat by (Berens, 2009)); a neuron was classified as 'gain' if its tuning depths were significantly different between interception and static condition (two-tailed Wilcoxon signed rand test, $p<0.05$); a neuron was classified as 'baseline' if its baseline activities were significantly different between interception and static condition (two-tailed Wilcoxon signed rand test, $p<0.05$).

Population decoding

The population activity of the motor cortex was used to decode target speed and reach direction by support vector machine (SVM). Neuronal firing rate was soft-normalized as

$$Fr_{norm.} = \frac{Fr_{raw}}{Fr_{max} - Fr_{min} + 5}$$

where raw firing rates was divided by the range of firing rates plus five (Churchland et al., 2012). We respectively trained two SVM classifiers (MATLAB function 'fitcecoc', 10-fold cross-validation) to decode reach direction (one in eight) and target speed (one in five) of single trials in 100-ms sliding window with 50-ms stride step. The temporal decoding procedure was repeated ten times to obtain the mean and standard deviation of decoding accuracy (Figure 3A). Then, we tested the generalization of groups of reach-direction and target-speed decoders (SVM, MATLAB function 'fitcecoc', 10-fold cross-validation) in different conditions. For this purpose, three epochs were selected as 200~400 ms after TO (TO + [200~400] ms), 200 ms around GO (GO ± 100 ms), and 200 ms around MO (MO ± 100 ms), and single-trial normalized population activity was averaged according to both conditions and

599 epochs. The reach-direction decoder, which was trained by a particular target-
600 speed condition in each epoch, was tested with trials from other target-speed
601 condition trials in different epochs. Similarly, the target-speed decoder, which
602 was trained by a given reach direction condition in each epoch, was tested
603 with trials from other reach-direction condition trials in different epochs. The
604 decoding accuracy for generalization is shown in confusion matrices (Figure
605 3B).

606 **Neural state**

607 The population activity was stored in NKT datasets, where N was the number
608 of neurons, K was the number of trials, and T was the number of time bins.
609 Neural activity was normalized by Z-score (MATLAB function 'zscore'). To
610 obtain the neural states at a given time point, neural activity was averaged for
611 relevant time bins (e.g. the two 50-ms bins around MO) to result in a K*N
612 dataset. After preprocessing, we used PCA to reduce the dimension from K*N
613 to K*C (C was the number of principal components). In the space spanned by
614 the first three PCs, neural states of single trials were colored in target speed
615 or reach direction (Figure 3C). All ellipse fitting was performed in three-
616 dimensional space. To show the condition-dependent neural structure more
617 clearly, we also projected neural states into the space of static condition
618 (Figure 4).

619 **RNN training**

620 In this procedure, motor intention appeared after GO and was represented as
621 fixed variables in forms of two-dimensional coordinates, cosine of reach
622 direction, or reach direction itself. We also tried an alternative form as
623 updating two-dimensional coordinates, which changed with time. Target
624 location was designed as real-time two-dimensional coordinates as well as
625 cosine or angle of real-time target direction, while the Go-signal was a step
626 function from 1 to 0 or a 10-ms pulse. The RNN in Figure 5 received motor
627 intention as stable two-dimensional coordinates, target location as real-time
628 cosine, and GO-signal as a step function. All trained RNNs were of 200
629 hidden units and to output hand velocity for accurate interception.

630 We built the three-layer RNNs with nodes according to standard dynamic
631 differential equation:

632 $$\tau\dot{x} = -x + Jr + Bu$$

where x means the activity, r means the firing rates, τ means time constant (50 ms). The connection matrix J of hidden layer is initiated as random in a normal distribution and the matrix B denotes the connection between inputs and hidden units. The output z is obtained by

$$z = Wr$$

where W is the read-out weight and is expected to reproduce the desired hand velocity generated by bell-shaped physical equation (Kao et al., 2021). During training, the loss function was:

$$E = e + \alpha r_1 + \beta r_2$$

where e means the mean squared error of z and training target. r_1 and r_2 are regularities (Sussillo et al., 2015), r_1 denotes the magnitude of input and readout weight and is calculated as their squared sum, while r_2 denotes the magnitude of the nodes' activity and is calculated as activity squared sum through time. For constants, $\alpha = 1e-3$ and $\beta = 1e-7$.

Single-neuron fitting and simulation

We used PD shift, gain, baseline, and full models to fit neuronal activity, based on cosine tuning. The gain model introduces nonlinear target-speed effects on the amplitude of cosine tuning as:

$$FR = \left(\frac{a_1}{1+e^{-a_2(sp.)}} + c_2\right) * cos\left(\theta - \theta_{pd}\right) + c_1$$

where FR is the firing rate at movement onset (MO ± 100 ms). θ and *sp*. Is the reach direction and target speed, respectively. θ_{pd} is the fitted preferred direction of the neuron. a_1, a_2, c_1 are constants to be fitted. Neurons are fitted by single-trial data.

In the PD shift model, the target-speed effects on PDs as:

$$FR = a_1 * cos\left(\theta - \theta_{pd} + \frac{a_3}{1 + e^{-a_2(sp.)}}\right) + c_1$$

with the similar symbols to gain model and a new constant a_3.

In the baseline model, the target speed adjusts the baseline activity:

$$FR = a_1 * cos\left(\theta - \theta_{pd}\right) + \frac{a_3}{1+e^{-a_2(sp.)}} + c_1$$

with similar symbols to above models.

662 The full model integrates all the three above effects:

663 $$FR = a_1 * cos(\theta - pd_{sp}) + \frac{a_2}{1 + e^{-a_2(\boldsymbol{sp}.)}} + \frac{a_3}{1 + e^{-a_2(\boldsymbol{sp}.)}} * cos(\theta - pd_{sp}) + a_4$$

664 $$* cos\left(\theta - pd_{sp} - \frac{a_5}{1 + e^{-a_2(\boldsymbol{sp}.)}}\right) + c_1$$

665 with constants a_1, a_2, a_3, a_4, a_5.

666 We fitted neuronal activity with these four models (MATLAB 'fit' function)

667 and compared the fitting goodness with adjusted R-squares ($R^2_{adj.} =$

668 $\frac{(1-r^2)(n-1)}{n-p-1}$, where n is the trial number, and p is the degree of the

669 polynomial).

670 Simulation with model neurons were based on these models to investigate

671 the relationship between neuronal tuning and population neural geometry.

672

673

References

Andersen, R.A., and Buneo, C.A. (2002). Intentional maps in posterior parietal cortex. Annu Rev Neurosci *25*, 189-220. 10.1146/annurev.neuro.25.112701.142922.

Andersen, R.A., and Cui, H. (2009). Intention, action planning, and decision making in parietal-frontal circuits. Neuron *63*, 568-583. 10.1016/j.neuron.2009.08.028.

Battaglia-Mayer, A., and Caminiti, R. (2019). Corticocortical Systems Underlying High-Order Motor Control. J Neurosci *39*, 4404-4421. 10.1523/jneurosci.2094-18.2019.

Berens, P.J.J.o.S.S. (2009). CircStat: AMATLABToolbox for Circular Statistics. *31*.

Churchland, M.M., Cunningham, J.P., Kaufman, M.T., Foster, J.D., Nuyujukian, P., Ryu, S.I., and Shenoy, K.V. (2012). Neural population dynamics during reaching. Nature *487*, 51-56. 10.1038/nature11129.

Churchland, M.M., Cunningham, J.P., Kaufman, M.T., Ryu, S.I., and Shenoy, K.V. (2010). Cortical preparatory activity: representation of movement or first cog in a dynamical machine? Neuron *68*, 387-400. 10.1016/j.neuron.2010.09.015.

Churchland, M.M., Yu, B.M., Ryu, S.I., Santhanam, G., and Shenoy, K.V. (2006). Neural variability in premotor cortex provides a signature of motor preparation. J Neurosci *26*, 3697-3712. 10.1523/JNEUROSCI.3762-05.2006.

Cisek, P., and Kalaska, J.F. (2005). Neural correlates of reaching decisions in dorsal premotor cortex: specification of multiple direction choices and final selection of action. Neuron *45*, 801-814. 10.1016/j.neuron.2005.01.027.

Cui, H. (2016). Forward Prediction in the Posterior Parietal Cortex and Dynamic Brain-Machine Interface. Frontiers in integrative neuroscience *10*, 35. 10.3389/fnint.2016.00035.

Dubreuil, A., Valente, A., Beiran, M., Mastrogiuseppe, F., and Ostojic, S. (2022). The role of population structure in computations through neural dynamics. Nat Neurosci *25*, 783-794. 10.1038/s41593-022-01088-4.

Evarts, E.V. (1968). Relation of pyramidal tract activity to force exerted during voluntary movement. J Neurophysiol *31*, 14-27. 10.1152/jn.1968.31.1.14.

Georgopoulos, A.P., Kalaska, J.F., Caminiti, R., and Massey, J.T. (1982). On the relations between the direction of two-dimensional arm movements and cell discharge in primate motor cortex. J Neurosci *2*, 1527-1537.

Hatsopoulos, N.G., and Suminski, A.J. (2011). Sensing with the motor cortex. Neuron *72*, 477-487. 10.1016/j.neuron.2011.10.020.

Inoue, Y., Mao, H., Suway, S.B., Orellana, J., and Schwartz, A.B. (2018). Decoding arm speed during reaching. Nature communications *9*, 5243. 10.1038/s41467-018-07647-3.

Kao, T.C., Sadabadi, M.S., and Hennequin, G. (2021). Optimal anticipatory control as a theory of motor preparation: A thalamo-cortical circuit model. Neuron *109*, 1567-1581.e1512. 10.1016/j.neuron.2021.03.009.

Kaufman, M.T., Churchland, M.M., Ryu, S.I., and Shenoy, K.V. (2014). Cortical activity in the null space: permitting preparation without movement. Nature neuroscience *17*, 440-448. 10.1038/nn.3643.

Li, Y., Wang, Y., and Cui, H. (2018). Eye-hand coordination during flexible manual interception of an abruptly appearing, moving target. J Neurophysiol *119*, 221-234. 10.1152/jn.00476.2017.

Li, Y., Wang, Y., and Cui, H. (2022). Posterior parietal cortex predicts upcoming movement in dynamic sensorimotor control. Proceedings of the National Academy of Sciences of the United States of America *119*, e2118903119. 10.1073/pnas.2118903119.

Merchant, H., Battaglia-Mayer, A., and Georgopoulos, A.P. (2003). Interception of real and apparent motion targets: psychophysics in humans and monkeys. Experimental brain research *152*, 106-112. 10.1007/s00221-003-1514-5.

Merchant, H., Battaglia-Mayer, A., and Georgopoulos, A.P. (2004a). Neural responses during interception of real and apparent circularly moving stimuli in motor cortex and area 7a. Cerebral cortex (New York, N.Y. : 1991) *14*, 314-331. 10.1093/cercor/bhg130.

Merchant, H., Battaglia-Mayer, A., and Georgopoulos, A.P. (2004b). Neural responses in motor cortex and area 7a to real and apparent motion. Experimental brain research *154*, 291-307. 10.1007/s00221-003-1664-5.

Moran, D.W., and Schwartz, A.B. (1999). Motor cortical representation of speed and direction during reaching. J Neurophysiol *82*, 2676-2692. 10.1152/jn.1999.82.5.2676.

Omrani, M., Kaufman, M.T., Hatsopoulos, N.G., and Cheney, P.D. (2017). Perspectives on classical controversies about the motor cortex. J Neurophysiol *118*, 1828-1848. 10.1152/jn.00795.2016.

Paninski, L., Fellows, M.R., Hatsopoulos, N.G., and Donoghue, J.P. (2004). Spatiotemporal tuning of motor cortical neurons for hand position and velocity. J Neurophysiol *91*, 515-532. 10.1152/jn.00587.2002.

Pesaran, B., Nelson, M.J., and Andersen, R.A. (2006). Dorsal premotor neurons encode the relative position of the hand, eye, and goal during reach planning. Neuron *51*, 125-134. 10.1016/j.neuron.2006.05.025.

Pouget, A., and Snyder, L.H. (2000). Computational approaches to sensorimotor transformations. Nature neuroscience *3 Suppl*, 1192-1198. 10.1038/81469.

Remington, E.D., Narain, D., Hosseini, E.A., and Jazayeri, M. (2018). Flexible Sensorimotor Computations through Rapid Reconfiguration of Cortical Dynamics. Neuron *98*, 1005-1019 e1005. 10.1016/j.neuron.2018.05.020.

Shenoy, K.V., Sahani, M., and Churchland, M.M. (2013). Cortical control of arm movements: a dynamical systems perspective. Annu Rev Neurosci *36*, 337-359. 10.1146/annurev-neuro-062111-150509.

Sobinov, A.R., and Bensmaia, S.J. (2021). The neural mechanisms of manual dexterity. Nature reviews. Neuroscience *22*, 741-757. 10.1038/s41583-021-00528-7.

763 Stavisky, S.D., Kao, J.C., Ryu, S.I., and Shenoy, K.V. (2017). Trial-by-Trial
764 Motor Cortical Correlates of a Rapidly Adapting Visuomotor Internal Model. J
765 Neurosci *37*, 1721-1732. 10.1523/jneurosci.1091-16.2016.

766 Sussillo, D., Churchland, M.M., Kaufman, M.T., and Shenoy, K.V. (2015). A
767 neural network that finds a naturalistic solution for the production of muscle
768 activity. Nature neuroscience *18*, 1025-1033. 10.1038/nn.4042.

769 Tanaka, H. (2016). Modeling the motor cortex: Optimality, recurrent neural
770 networks, and spatial dynamics. Neuroscience research *104*, 64-71.
771 10.1016/j.neures.2015.10.012.

772 Tkach, D., Reimer, J., and Hatsopoulos, N.G. (2007). Congruent activity
773 during action and action observation in motor cortex. J Neurosci *27*, 13241-
774 13250. 10.1523/jneurosci.2895-07.2007.

775 Vyas, S., Golub, M.D., Sussillo, D., and Shenoy, K.V. (2020). Computation
776 Through Neural Population Dynamics. Annu Rev Neurosci *43*, 249-275.
777 10.1146/annurev-neuro-092619-094115.

778 Wang, T., Chen, Y., and Cui, H. (2022). From parametric representation to
779 dynamical system: shifting views of the motor cortex in motor control.
780 Neuroscience Bulletin *38*, 796-808. 10.1007/s12264-022-00832-x.

781 Zipser, D., and Andersen, R.A. (1988). A back-propagation programmed
782 network that simulates response properties of a subset of posterior parietal
783 neurons. Nature *331*, 679-684. 10.1038/331679a0.

784